Supporting Information

Oxygen-deficient titanium dioxide as a functional host

for lithium-sulfur batteries

Hong-En Wang,[a] Kaili Yin,[a] Ning Qin,[c] Xu Zhao,[d] Fan-Jie Xia,[a] Zhi-Yi Hu,[a] Guanlun

Guo,[*f] Guozhong Cao[*e] and Wenjun Zhang[*b]

[a] State Key Laboratory of Advanced Technology for Materials Synthesis and

Processing, Wuhan University of Technology, Wuhan 430070, China.

[b] Center of Super Diamond & Advanced Films (COSDAF) and Department of

Materials Science and Engineering, City University of Hong Kong, HKSAR, China.

Email: apwjzh@cityu.edu.hk

[c] Department of Materials Science and Engineering, Southern University of Science

and Technology, Shenzhen 518055, China.

[d] Institute of Chemical Materials, China Academy of Engineering Physics, Mianyang

621900, China.

[e] Department of Materials Science and Engineering, University of Washington, Seattle,

WA 98195, USA. Email: gzcao@u.washington.edu

[f] Hubei Key Laboratory of Advanced Technology for Automotive Components, Wuhan

University of Technology, Wuhan 430070, China. Email: glguo@whut.edu.cn

Experimental section

All chemicals were analytical grade and used without any further purifications.

Synthesis of TiO_2/oleylamine hybrid.

The synthesis of TiO_2/oleylamine (OA) particles referred to previous work[1] with little modification. In a typical procedure, 4.5 mL tetrabutyl titanate was rapidly added into 200 mL ethanol containing 0.8 mL deionized (DI) water and 1.8 mL oleylamine under vigorous stirring. The NH_2- group of OA can complex with TiO_2 *via* intermolecular hydrogen-bonding. Meantime, long-chain alkyl groups of OA tend to self-assemble and aggregate by van der Waals interaction, leading to formation of spherical TiO_2/OA particles with reduced surface energy of the total system. After aging statically for 2 h, the resulting precipitates were collected by centrifugation, washed with ethanol for 3 times and finally dried at 60 °C in air. The TiO_2/OA then served as precursor (Scheme 1a) for synthesis of TiO_2-Ar and TiO_2-air samples in the following procedure.

Synthesis of TiO_2-Ar and TiO_2-air samples.

The mesoporous TiO_2 was prepared by hydrothermal reaction of 0.2 g TiO_2/OA precursor in a mixture of 40 mL ethanol and 20 mL H_2O in 100 mL Teflon-lined autoclave at 160 °C for 12 h. During this process, amorphous TiO_2 colloids in the hybrid were crystallized into mesoporous anatase; meantime, trace residual OA was *in situ* capped on the TiO_2 surface (Scheme 1b). The resultant TiO_2 product was rinsed with ethanol and distilled water in sequence, and finally dried at 60 °C in air. Then, the TiO_2 powders were annealed in a tube furnace at 500 °C for 2 h purged with floating Ar, and then naturally cooled to room temperature to obtain mesoporous oxygen-deficient TiO_2

(denoted as "TiO$_2$-Ar", Scheme 1c). In contrast, pure mesoporous TiO$_2$ was harvested after annealing at 500 °C for 2 h in air (denoted as "TiO$_2$-air", Scheme 1d).

Preparation of TiO$_2$-Ar/S and TiO$_2$-air/S composite cathodes.

The composite sulfur cathodes were prepared by loading sulfur into the mesoporous TiO$_2$-Ar and TiO$_2$-air, respectively by a conventional melt-diffusion method with little modification. Typically, sulfur powders (300 mg) were dissolved in 10 mL CS$_2$ containing 200 mg of TiO$_2$-Ar (or TiO$_2$-air) powders. The mixture was continuously stirred for 8 h and then dried at 40 °C for 12 h until CS$_2$ solvent was thoroughly evaporated. Finally, the resulting composites were sealed in a Teflon-lined autoclave and maintained at 155 °C for 12 h, followed by naturally cooling to room temperature.

Physical characterizations.

Powder X-ray diffraction (XRD) patterns were recorded on a Bruker diffractometer with Cu Kα radiation at 40 kV/mA. Thermogravimetric (TG) analysis was carried out using a thermal analyzer (Setaram, Labsys Evo) in air (for the determination of carbon content in TiO$_2$-Ar) or in Ar atmosphere (for the measurement of sulfur contents in TiO$_2$-Ar/S and TiO$_2$-air/S) with a temperature ramp rate of 5 °C min^{-1}. The morphology and particle size of the samples were observed by a field-emission scanning electron microscope (SEM, Hitachi S-4800). N$_2$ adsorption/desorption isotherms were recorded on a Micrometrics, TriStar II 3020 system at 77 K. Prior to adsorption, the samples were degassed for 12 h at 100 °C in vacuum. Transmission electron microscopy (TEM) and high-resolution TEM (HRTEM) micrographs were acquired on a JEM-2100F transmission electron microscope operated at 200 kV. High angle annular dark field

scanning transmission electron microscopy (HAADF-STEM) images and energy-dispersive X-ray (EDX) patterns were obtained from an FEI Talos microscope fitted with super-X EDX system operated at 200 kV. The surface composition and element valence states of the samples were analyzed using an X-ray photoelectron spectroscope (XPS, Thermo Fisher Scientific, Alpha) using a monochromatic Al K_α radiation source at 15 kV (1486.71 eV). The XPS peak positions locations were calibrated using the C 1s peak reference of adventitious carbon at 284.8 eV. Spectral deconvolution was performed using the XPS Peak 4.1 software. Electron paramagnetic resonance (EPR) signals were collected using a Bruker EMX plus-10/12 with a Microwave Bridge (microwave frequency: 9.853 GHz; power: 20 mW; modulation amplitude: 4 G; modulation frequency: 200 kHz) at room temperature. The contact angle measurements were performed using an OCA35 automatic contact angle instrument.

Polysulfide adsorption experiments.

Sulfur and Li_2S powders with a 5:1 molar ratio were added to a 1 : 1 (v/v) 1,3-dioxolane (DOL) and 1,2-dimethoxyethane (DME) mixture and stirred overnight at 60 °C. The as-prepared Li_2S_6 solution (0.5 mM) was used as the stock solution for adsorption measurements. 20 mg TiO_2-Ar or TiO_2-air powder was added to 5 mL each of the Li_2S_6 stock solution. The mixture was vigorously stirred to facilitate adsorption, followed by keeping at static for 12 h at room temperature.

Electrochemical tests.

Electrochemical performances were measured using coin-type CR2025 cells with Li foil as counter and reference electrodes at room temperature. The working electrodes were prepared by thoroughly blending the active materials (TiO_2-Ar/S or TiO_2-air/S),

carbon black (super-P) and polyvinylidene difluoride (PVDF) binder with 8:1:1 weight ratio in N-methyl-2-pyrrolidone (NMP) solvent. The resulting slurry was pasted on an Al foil, dried at 55 °C for 12 h in vacuum and then punched into circular disk electrodes. 1.0 M lithium bis(trifluoromethanesulfonyl)imide (LiTFSI) dissolved in 1,3-dioxalane (DOL) and dimethyl ether (DME) (1:1 v/v) with 1 wt% $LiNO_3$ additive was used as the working electrolyte. The assembling of the Li-S cells was operated in an Ar-filled glove-box with water and oxygen contents below 1 ppm. Cyclic voltammetry (CV) was recorded on CHI660E (Shanghai Chenhua instrument Co., Ltd) electrochemical workstation within a potential window of 1.8~2.8 V vs. Li^+/Li at 0.1 mV s^{-1}. Galvanostatic charge/discharge tests were carried out on a LAND CT2001A test instrument (Wuhan) at current rates of 0.2~5 C (1 C = 1675 mA g^{-1}). The specific capacities were calculated based on the weight of sulfur in the composite cathodes. Electrochemical impedance spectra (EIS) were measured at open-circuit potential with an electrochemical workstation (Autolab PGSTAT 302N) in the frequency range from 100 kHz to 10 mHz with an amplitude of 10 mV.

Computational details.

First-principles density functional theory (DFT) calculations were performed using CASTEP in Materials Studio.[2, 3] The exchange and correlation energies were calculated using OTFG ultrasoft pseudopotential and Perdew–Burke–Ernzerhof (PBE) functional within the generalized gradient approximation (GGA). The electron-ion interactions were described within a plane-wave basis set with an energy cutoff of 580 eV. A $2\times3\times1$ supercell containing 90 atoms was used to model the electronic structures of bulk anatase. To correct the on-site electron correlation, GGA plus Hubbard model (GGA+U) has been employed with U = 7.5 eV.[4] To simulate the surface electronic structures, a

TiO$_2$ (100) surface slab was cleaved and a vacuum layer of 20 Å was used to avoid the unwanted interactions between neighboring cells along z-direction. For simulations of oxygen-deficient anatase bulk anatase or surface, one O atom was removed from the supercell or (100) surface slab, respectively. The convergence tests of the total energy with respect to the k-points sampling and the energy-cutoff were carefully examined, using 2×2×1 Monkhorst-Pack k-points grid for TiO$_2$ bulk and 1×1×1 k-points for the pristine surface slabs and adsorption with Li$_2$S$_4$ or Li. Ionic relaxations were performed using a conjugate gradient algorithm until the net force on all individual atoms was less than 0.03 eV Å^{-1}, the SCF tolerance was set to 1×e^{-6} eV·atom^{-1} for geometry optimization.

The adsorption energy (E_{ad}) for Li$_2$S$_4$ or Li on TiO$_2$ surface is determined using the following equation:

$$E_{ad} = E_{total} - E_{surf} - E_{mol}$$

where E_{total} is the total energy of the system containing TiO$_2$ (001) surface with adsorbed Li$_2$S molecule (or Li$^+$), E_{surf} is the energy of the clean TiO$_2$ (001) surface with or without $V_o^{\bullet\bullet}$, E_{mol} is the energy of a free Li$_2$S$_4$ molecule or Li. During E_{ad} calculations, van der Waals interactions were included. The Li diffusion on TiO$_2$ (001) surface slab was simulated using a complete linear synchronous transit/quadratic synchronous transit (LST/QST) method.
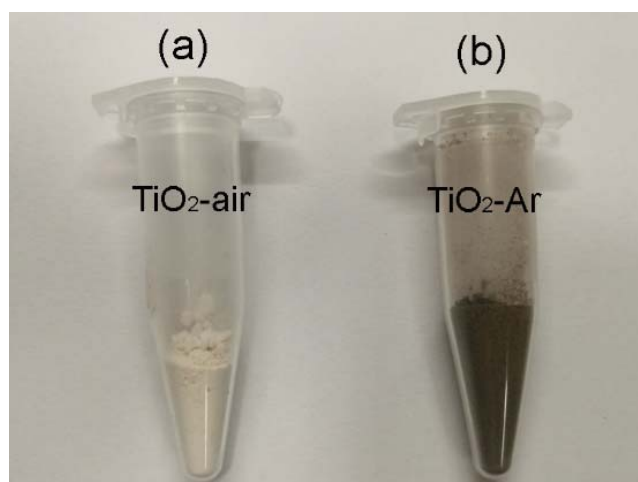
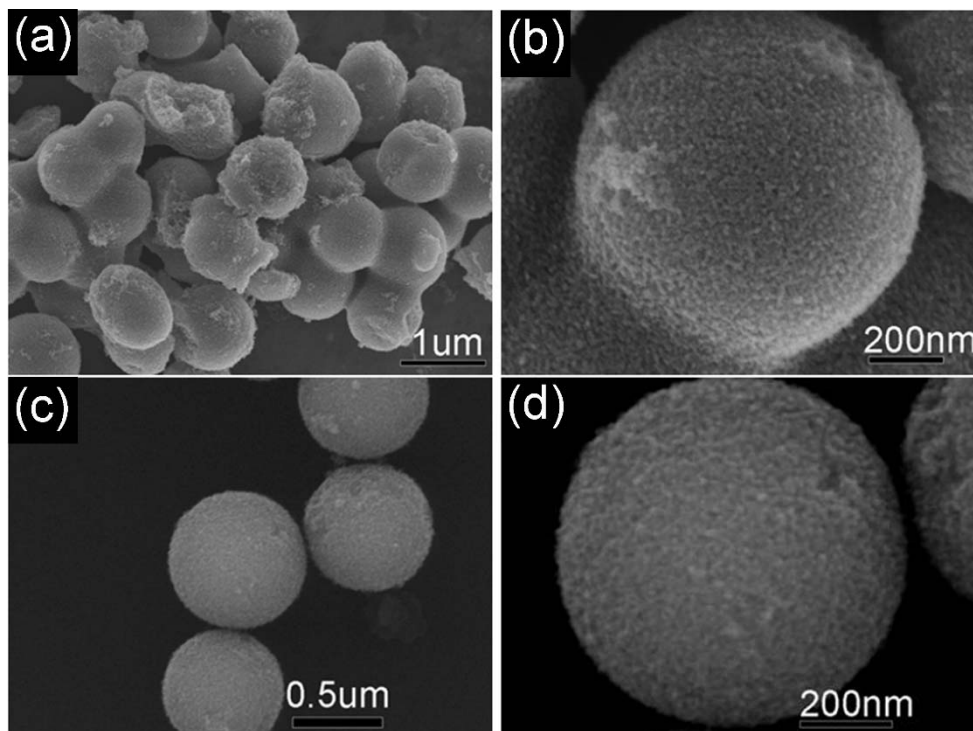**Fig. S1** Digital photos of the porous (a) TiO_2-air and (b) TiO_2-Ar samples.

Fig. S2 SEM images of the as-prepared TiO$_2$ samples. (a, b) TiO$_2$-Ar, (c, d) TiO$_2$-air.
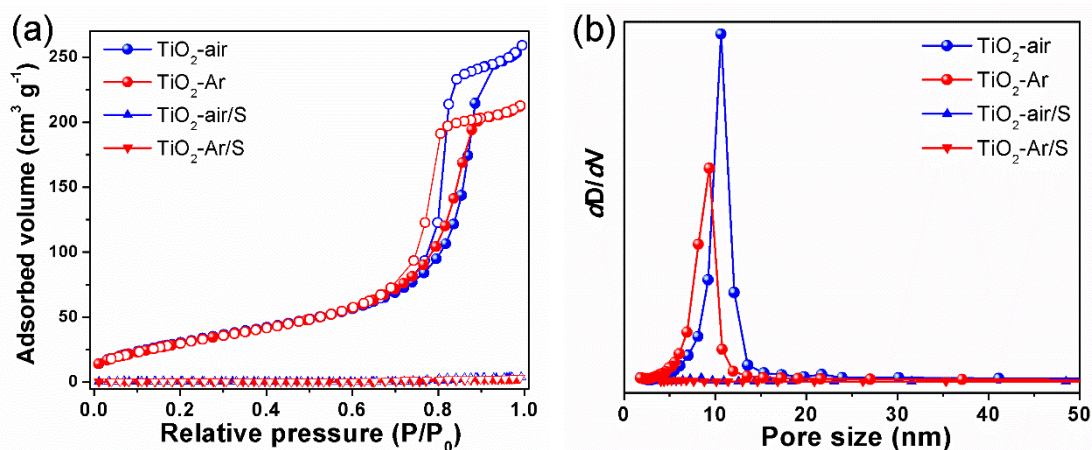
Fig. S3 (a) N$_2$ sorption isotherms and (b) pore size distribution plots of TiO$_2$-Ar, TiO$_2$-air, TiO$_2$-Ar/S and TiO$_2$-air/S samples.

From Fig. S3a, the TiO$_2$-Ar and TiO$_2$-air both possess high specific surface areas of 118 and 121 m^2 g^{-1}, respectively, due to their interconnected mesoporous structure. However, after sulfur filling the specific surface areas of the resultant TiO$_2$-Ar/S and TiO$_2$-air/S composites are sharply reduced to ~1.3 m^2 g^{-1} and 1.2 m^2 g^{-1} respectively, suggesting the full occupation of inner voids by sulfur species.
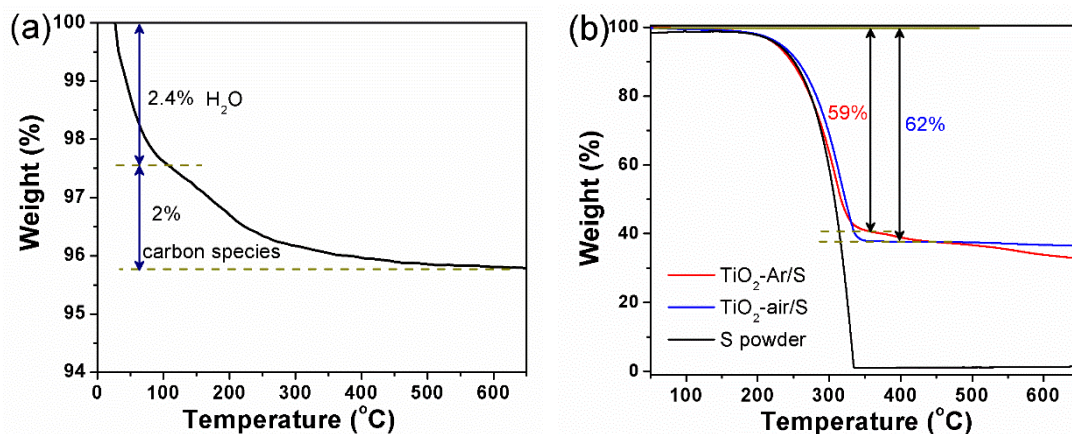
Fig. S4 TG analyses of (a) TiO_2-Ar sample in air and (b) TiO_2-Ar/S, TiO_2-air/S and bare S powders in N_2, respectively.

Thermogravimetric (TG) measurements are used to determine the weight fraction of carbon species in the TiO_2-Ar sample. In Fig. S4a, the weight loss of ~2.4 wt % before 100 °C is mainly caused by the desorption of physically adsorbed H_2O on the surface. The second weight drop of ca. 2 wt% between 200 and 600 °C corresponds to the decomposition of the carbon species. Herein, a higher temperature of ~600 °C is required for the complete removal of carbon compared to recent literature (~480 °C)[5] which can be mainly ascribed to the trap of most carbon inside the mesopores and formation of Ti-C chemical bonds.[6]

TG curves of TiO_2-Ar/S, TiO_2-air/S and pure S powders are presented in Fig. S4b. The weight loss for the 3 samples all occurs between 170 and 350 °C caused by sulfur sublimation. The corresponding weight fractions of sulfur in TiO_2-Ar/S and TiO_2-air/S are calculated to be 59% and 62% respectively, which are near to the setting mass ratios.
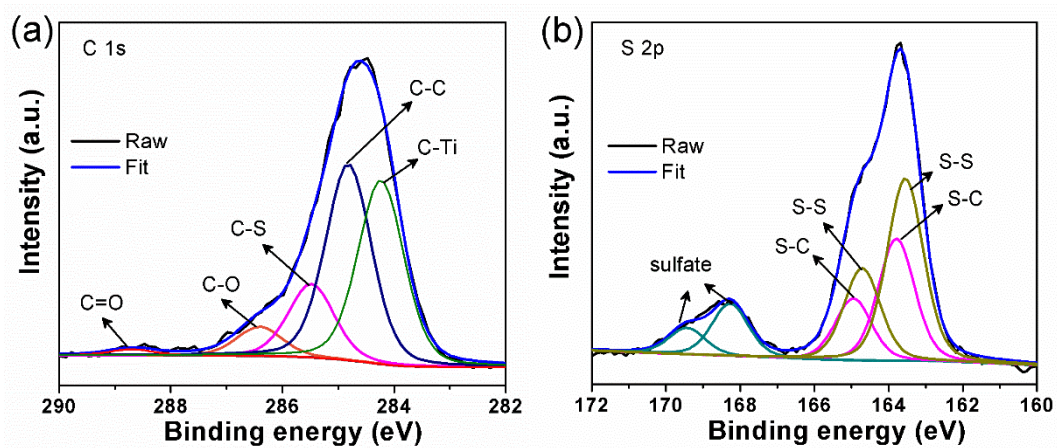
Fig. S5 High-resolution XPS spectra of (a) C 1s and (b) S 2p spectra in TiO$_2$-Ar/S.

The existence of C-C, C-O and C=O bonds stems from minority amorphous carbon with surface functional groups that was produced by carbonization of residual oleylamine. The C-Ti peak in C 1s spectrum further supports the formation of Ti-C bonding at TiO$_2$/C interface.[6]
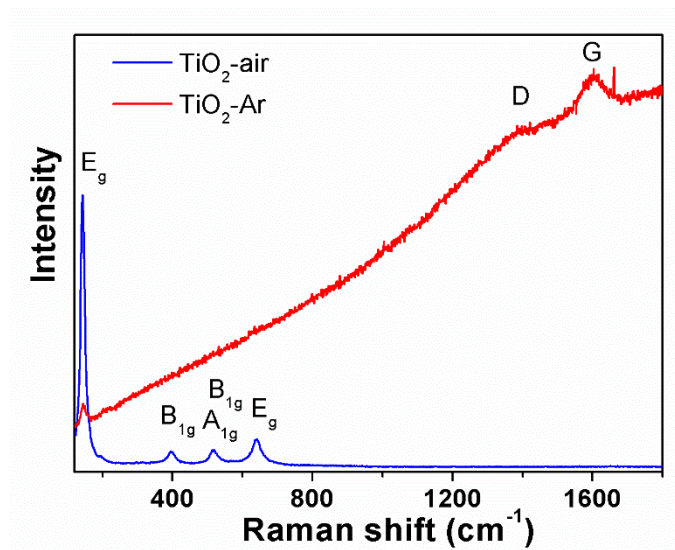
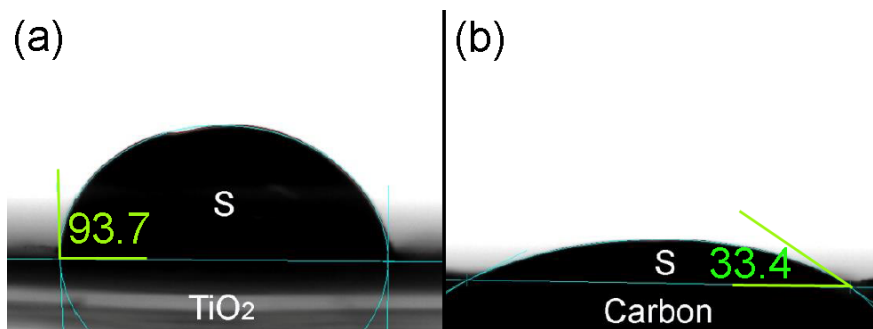**Fig. S6** Raman spectra of TiO$_2$-Ar and TiO$_2$-air samples.

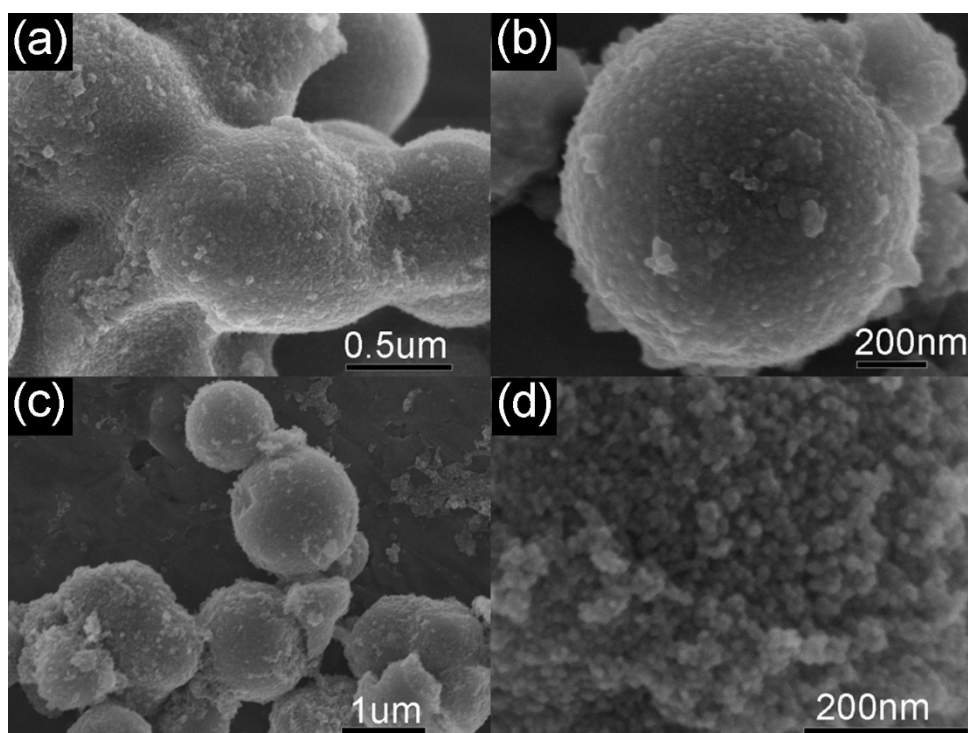**Fig. S7** Contact angle measurements of melted sulfur on (a) TiO$_2$ and (b) carbon surface, respectively.

Fig. S8 SEM images of (a, b) TiO$_2$-Ar/S and (c, d) TiO$_2$-air/S samples.
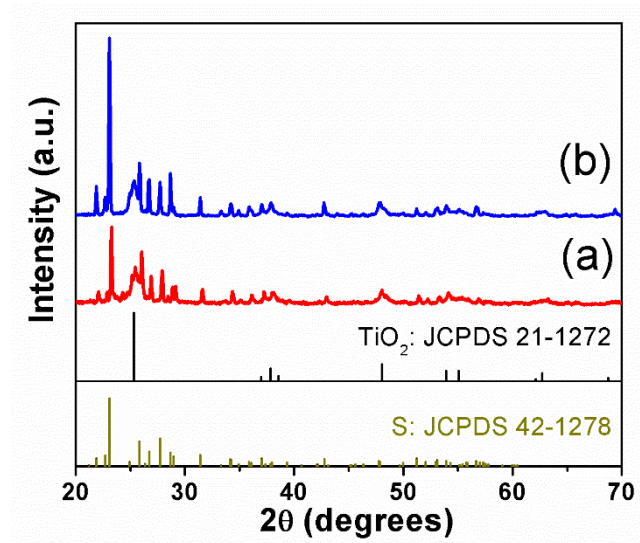
Fig. S9 XRD patterns of (a) TiO$_2$-Ar/S and (b) TiO$_2$-air/S samples.
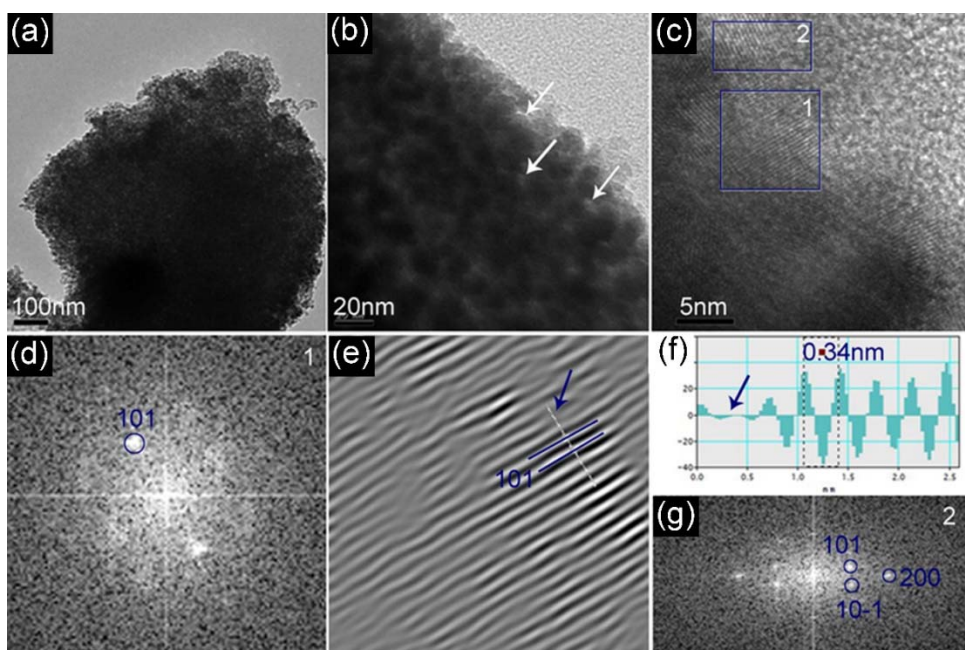
Fig. S10 TEM characterizations of the TiO$_2$-Ar/S sample. (a) TEM image; (b) magnified view revealing few mesopores (marked by white arrows); (c) HRTEM; (d) FFT pattern of region 1 in (c); (e) IFFT image derived from (101) spots in (d); (f) intensity of line profile (marked by white in (e)); (g) FFT pattern of region 2 in (c).

TEM images (Fig. S10a and b) depict that the spherical morphology and mesoporous structure of TiO$_2$-Ar have been preserved after S impregnation. HRTEM micrograph and corresponding FFT patterns (Fig. S10c, d, g) reveal the presence of anatase. In addition, some dislocations can be discerned as marked by blue arrows (Fig. S10e and f). The intensity of line profile (Fig. S10f) displays a large change in the contrast from the right/central regions to the left edge position, reflecting the presence of structural distortion possibly caused by oxygen loss from TiO$_2$ lattice and compressive stress at TiO$_2$/C interface.[7] The absence of crystalline S can be due to its poor stability and easy sublimation under intensive e-beam irradiation in vacuum.
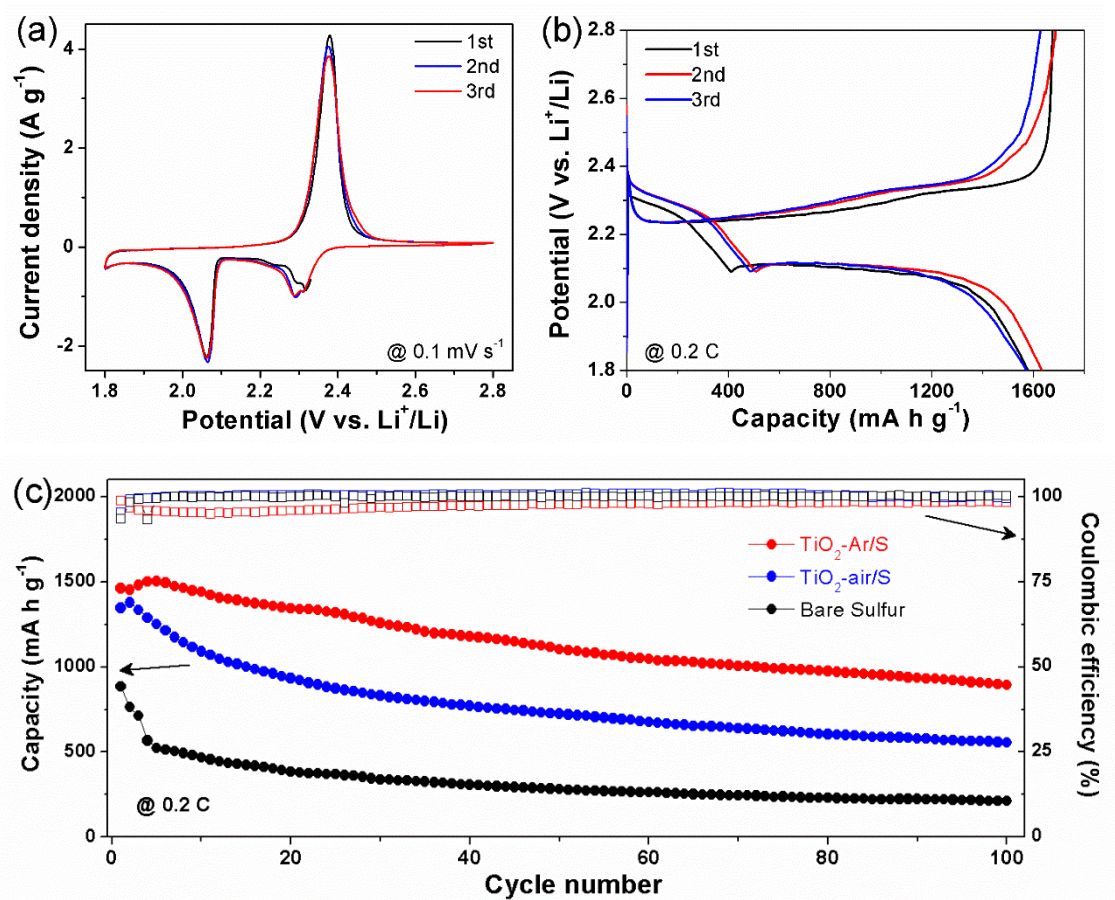
Fig. S11 (a) cyclic voltammetry curves and (b) galvanostatic charge-discharge curves of TiO$_2$-Ar/S electrode in the initial 3 cycles. (c) cycling performance the 3 electrodes at 0.2 C (1 C = 1675 mA g^{-1}).

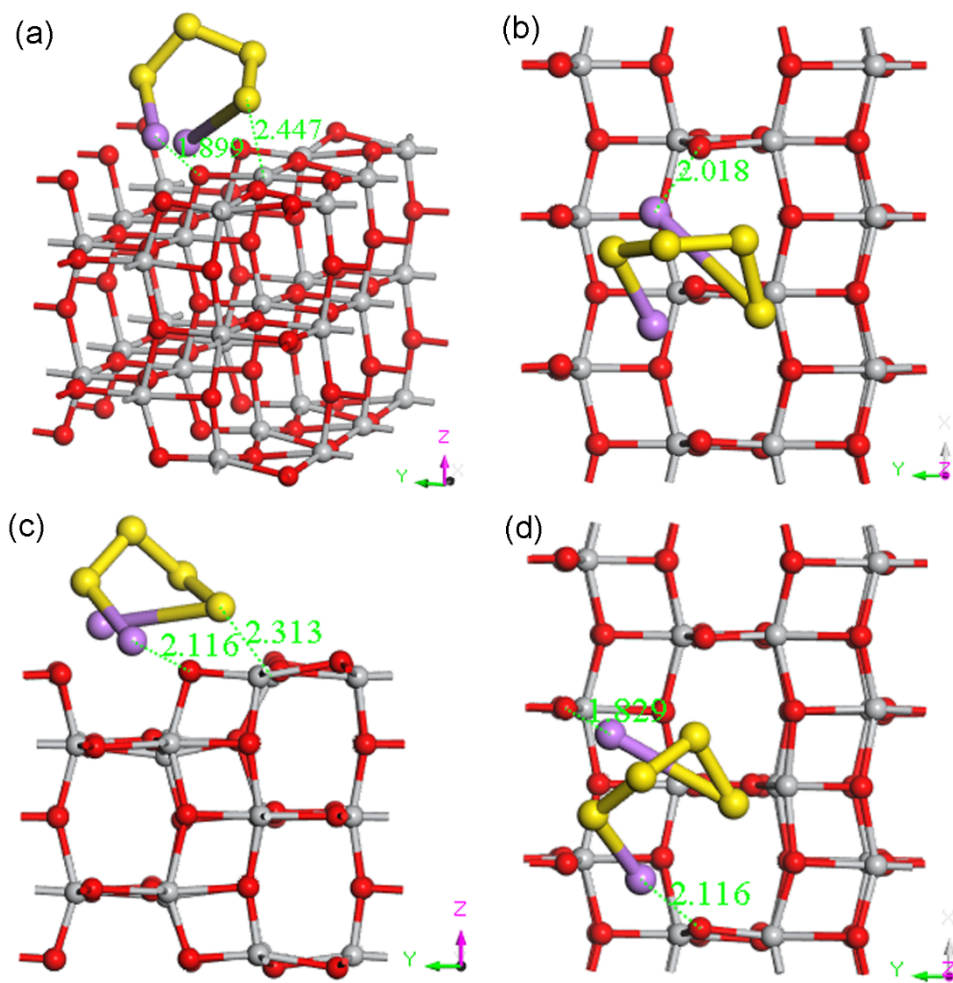**Fig. S12** Optimized adsorption configurations of Li$_2$S$_4$ on anatase (100) slab surface without (a, b) and with (c, d) $V_o^{\bullet\bullet}$. The grey, red, yellow and pink balls represent Ti, O, S and Li, respectively.
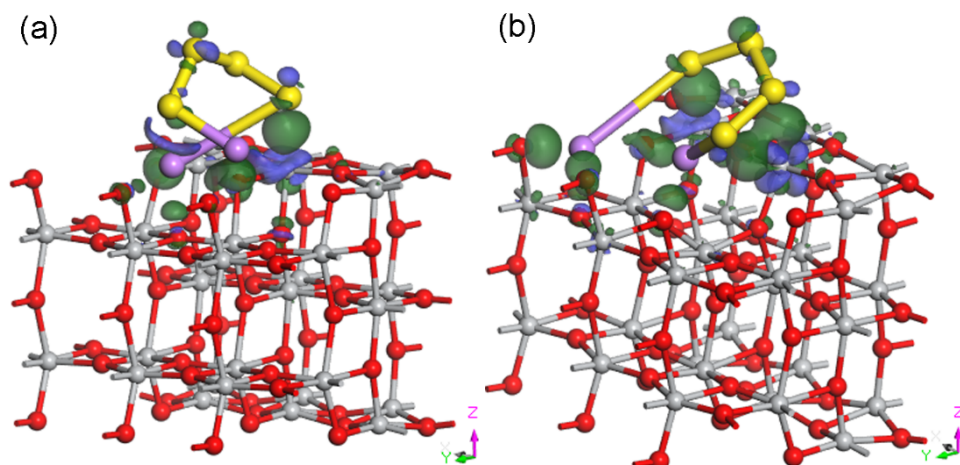
Fig. S13 Optimized geometry structures and corrsponding charge density distribution contours of Li_2S_4 adsorbed on anatase (100) slab surface without (a) and with (b) $V_o^{\bullet\bullet}$ (The green and blue contours signify the electron accummulation and depletion regions, respectively). The grey, red, yellow and pink balls represent Ti, O, S and Li atoms, respectively.
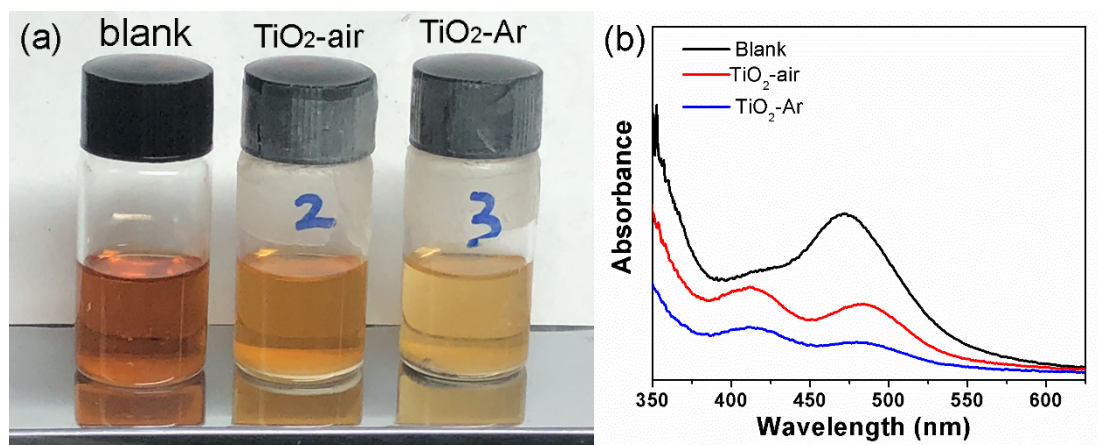
Fig. S14 (a) Digital photos of blank Li$_2$S$_6$ electrolyte and after adding TiO$_2$-air or TiO$_2$-Ar, respectively; (b) UV-vis absorption spectra of the supernatant separated from the Li$_2$S$_6$ solutions after adsorption experiments in (a).

In Fig. S14a, the color of the Li$_2$S$_6$ solution after adding TiO$_2$-Ar and TiO$_2$-air both fades, demonstrating their high affinity to polysulfides. In Fig. S14b, the UV-vis absorption peaks for supernatant from Li$_2$S$_6$ solutions with TiO$_2$-Ar greatly diminished compared to that with TiO$_2$-air, confirming the higher affinity of TiO$_2$-Ar to polysulfide.
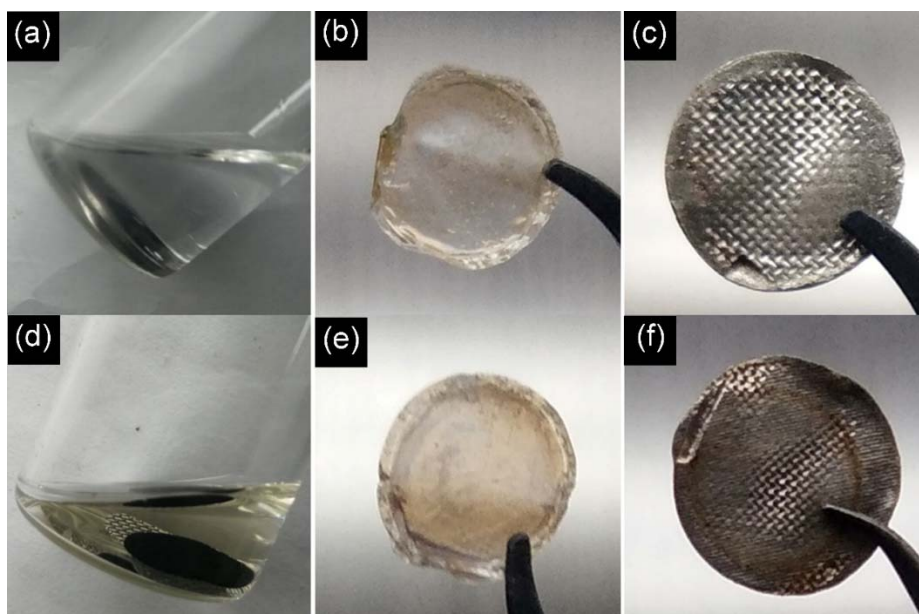
Fig. S15 Photographs of Li-S cells' components after 100 cycles at 0.2 C. (a, d) cathode soaked in fresh electrolyte; (b, e) separator; (c, f) Li anode. Images of (a-c) and (d-f) are taken from Li-S cells with TiO_2-Ar/S and TiO_2-air/S as cathodes, respectively.

In Fig. S15a, the electrolyte soaked with cycled TiO_2-Ar/S cathode remains colorless, suggesting no polysulfide formed or trace formed polysulfide has been tightly adsorbed at cathode surface. In contrast, the electrolyte with cycled TiO_2-air/S cathode changes to slightly yellow (Fig. S15d), hinting the possible formation of soluble polysulfides. In addition, both the separator and Li-anode coupled with TiO_2-Ar/S remain almost clean (Fig. S15b and c). Instead, some sulfide species are deposited on the surface of separator and Li-anode coupled with TiO_2-air/S (Fig. S15e and f), possibly due to the shuttling of polysulfide intermediates.
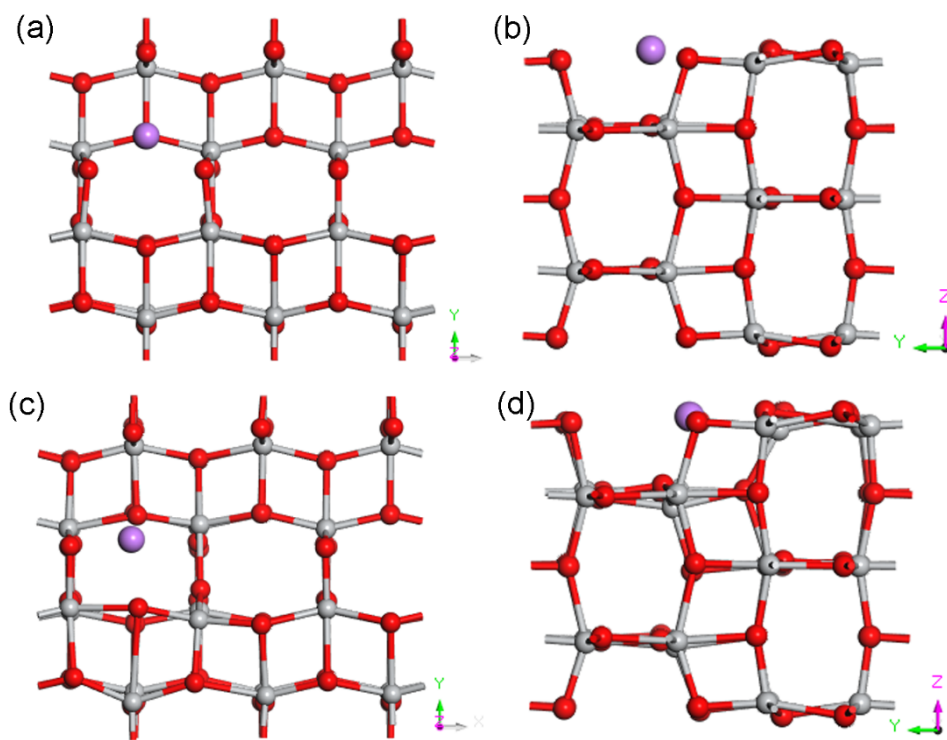
Fig. S16 Optimized adsorption positions of Li on anatase (100) slab surface of (a, b) without and with (c, d) $V_o^{\bullet\bullet}$. (a, c) tope view, (b, d) side view. The grey, red, and pink balls represent Ti, O, and Li, respectively.
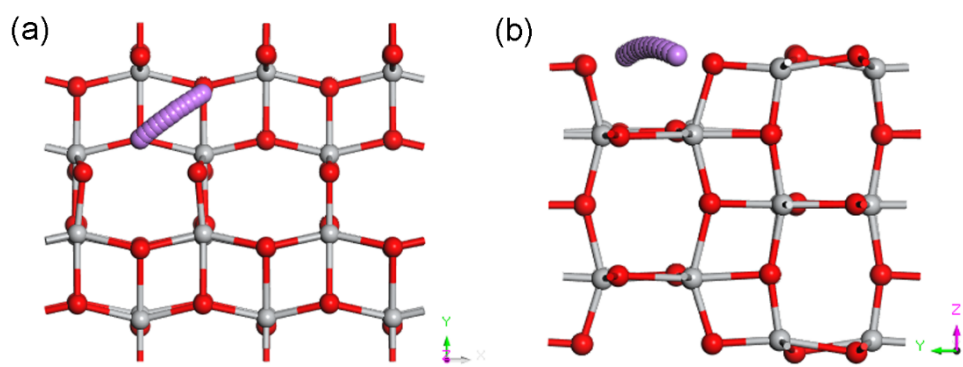
Fig. S17 Li diffusion paths on TiO$_2$ (100) slab without $V_o^{\bullet\bullet}$. (a) top and (b) side view.

Table S1. Summary of pore characteristics of the as-synthesized samples.

	TiO$_2$-Ar	TiO$_2$-air	TiO$_2$-Ar/S	TiO$_2$-air/S
BET (m^2 g^{-1})	118	121	1.3	1.2
Pore volume (cm^3 g^{-1})	0.58	0.6	-	-
Average pore size (nm)	9.4	10.6	-	-

Table S2. Rate performance comparison of our work with recent literature of Li-S batteries using other cathode hosts.

| Cathode hosts	Capacity (mA h g^{-1}) 0.5 C	Capacity (mA h g^{-1}) 1 C	Capacity (mA h g^{-1}) 2 C	Capacity (mA h g^{-1}) 5 C
TiO_2 with $V_o^{\bullet\bullet}$ (This work)	**999**	**712**	**571**	**401**
Hollow C@TiO_2@C[8]	800	630	560	NA
Graphene aerogel/TiO_2[9]	707	664	606	333(4 C)
TiO_2@graphene+C[10]	682	534	426	165(3 C)
Magneli Ti_nO_{2n-1}@C[11]	801	700	NA	NA
mesoporous TiO_2[12]	576	520	445	NA
C@Ru particles[13]	790	610	420	NA
TiO_2-TiN junction[14]	710	600	480	NA
graphene/SnS_2/TiO_2[15]	697	563	499	306
rGO[16]	900	750	600	230
3DNG/TiO_2[17]	1000	800	600	200
N-C/MoS_2/CNT[18]	906	801.8	671.6	NA
MoS_2/hierarchical C spheres[19]	902	775	700	NA
MoS_2/rGO[20]	860	750	660	NA
SnS_2 dots/Graphene[21]	650	514	412	NA
C nanofibers/MnO_2[22]	859	565	NA	NA
Co-VN@C[23]	820	730	650	490

NA: not available

Table S3. Cyclability comparison of our work with other work of Li-S cells using other

cathode hosts.

Cathode hosts	Current rate (C)	Cycle number	Retained capacity ($mA\,h\,g^{-1}$)	Retention ratio (%)
TiO_2 with $V_O^{\bullet\bullet}$ (This work)	**0.2**	**100**	**900**	**61**
TiO_2 with $V_O^{\bullet\bullet}$ (This work)	**1.0**	**500**	**538**	**59**
Magneli Ti_nO_{2n-1}@C[11]	1.0	500	425	60
graphene/SnS_2/TiO_2[15]	0.2	100	739	65
MoS_2/rGO[24]	1.0	300	480	55
Graphene/Pt[25]	0.2	100	~700	~64
TiS_2[26]	0.3	100	~800	~50
rGO[16]	0.2	100	~700	~58
MoS_2/rGO[20]	1.0	300	480	55

NA: not available

References

1. D. Chen, L. Cao, F. Huang, P. Imperia, Y.-B. Cheng and R. A. Caruso, *J. Am. Chem. Soc.*, 2010, **132**, 4438-4444.
2. M. D. Segall, P. J. D. Lindan, M. J. Probert, C. J. Pickard, P. J. Hasnip, S. J. Clark and M. C. Payne, *J. Phys. Cond. Mat.*, 2002, **14**, 2717-2744.
3. S. J. Clark, M. D. Segall, C. J. Pickard, P. J. Hasnip, M. J. Probert, K. Refson and M. C. Payne, *Zeitschrift Fur Kristallographie*, 2005, **220**, 567-570.
4. J. Qiu, S. Li, E. Gray, H. Liu, Q.-F. Gu, C. Sun, C. Lai, H. Zhao and S. Zhang, *Journal of Physical Chemistry C*, 2014, **118**, 8824-8830.
5. H. B. Huang, Y. Yang, L. H. Chen, Y. Wang, S. Z. Huang, J. W. Tao, X. T. Ma, T. Hasan, Y. Li, Y. Xu and B. L. Su, *Nanoscale*, 2016, **8**, 10928-10937.
6. Y. Cai, H.-E. Wang, X. Zhao, F. Huang, C. Wang, Z. Deng, Y. Li, G. Cao and B.-L. Su, *ACS Appl. Mater. Interfaces*, 2017, **9**, 10652-10663.
7. Y. Yang, P. Gao, Y. Wang, L. Sha, X. Ren, J. Zhang, Y. Chen, T. Wu, P. Yang and X. Li, *Nano Energy*, 2017, **33**, 29-36.
8. M. Fang, Z. Chen, Y. Liu, J. Quan, C. Yang, L. Zhu, Q. Xu and Q. Xu, *J. Mater. Chem. A*, 2018, **6**, 1630-1638.
9. J.-Q. Huang, Z. Wang, Z.-L. Xu, W. G. Chong, X. Qin, X. Wang and J.-K. Kim, *ACS Appl. Mater. Interfaces*, 2016, **8**, 28663-28670.
10. X. Shang, P. Guo, T. Qin, M. Liu, M. Lv, D. Liu and D. He, *Adv. Mater. Interfaces*, 2018, **5**, 1701602.
11. U. Zubair, J. Amici, C. Francia, D. McNulty, S. Bodoardo and C. O'Dwyer, *Chemsuschem*, 2018, **11**, 1838-1848.
12. Y. Sun, Y. Zhao, Y. Cui, J. Zhang, G. Zhang, W. Luo and W. Zheng, *Electrochim. Acta*, 2017, **239**, 56-64.
13. R. Pongilat and K. Nallathamby, *ACS Appl. Mater. Interfaces*, 2018, **10**, 38853-38861.
14. T. Zhou, W. Lv, J. Li, G. Zhou, Y. Zhao, S. Fan, B. Liu, B. Li, F. Kang and Q.-H. Yang, *Energy Environ. Sci.*, 2017, **10**, 1694-1703.
15. L. Kong, X. Chen, B.-Q. Li, H.-J. Peng, J.-Q. Huang, J. Xie and Q. Zhang, *Adv. Mater.*, 2018, **30**, 1705219.
16. Z. Cheng, Z. Xiao, H. Pan, S. Wang and R. Wang, *Adv. Energy Mater.*, 2018, **8**, 1702337.
17. Z. Li, Q. He, X. Xu, Y. Zhao, X. Liu, C. Zhou, D. Ai, L. Xia and L. Mai, *Adv. Mater.*, 2018, **30**, 1804089.
18. J. Ren, Y. Zhou, L. Xia, Q. Zheng, J. Liao, E. Long, F. Xie, C. Xu and D. Lin, *J. Mater. Chem. A*, 2018, **6**, 13835-13847.
19. L. Hu, C. Dai, J.-M. Lim, Y. Chen, X. Lian, M. Wang, Y. Li, P. Xiao, G. Henkelman and M. Xu, *Chem. Sci.*, 2018, **9**, 666-675.
20. Y. You, Y. Ye, M. Wei, W. Sun, Q. Tang, J. Zhang, X. Chen, H. Li and J. Xu, *Chem. Eng. J.*, 2019, **355**, 671-678.
21. L. Luo, S.-H. Chung and A. Manthiram, *J. Mater. Chem. A*, 2018, **6**, 7659-7667.
22. Z. Liu, B. Liu, P. Guo, X. Shang, M. Lv, D. Liu and D. He, *Electrochim. Acta*,

2018, **269**, 180-187.

23. W. Ren, L. Xu, L. Zhu, X. Wang, X. Ma and D. Wang, *ACS Appl. Mater. Interfaces*, 2018, **10**, 11642-11651.

24. Y. You, Y. Ye, M. Wei, W. Sun, Q. Tang, J. Zhang, X. Chen, H. Li and J. Xu, *Chem. Eng. J.*, 2019, **355**, 671-678.

25. H. Al Salem, G. Babu, C. V. Rao and L. M. R. Arava, *J. Am. Chem. Soc.*, 2015, **137**, 11542-11545.

26. X.-C. Liu, Y. Yang, J. Wu, M. Liu, S. P. Zhou, B. D. A. Levi, X.-D. Zhou, H. Cong, D. A. Muller, P. M. Ajayan, H. D. Abruna and F.-S. Ke, *ACS Energy Lett.*, 2018, **3**, 1325-1330.